PERIODICO di MINERALOGIA
established in 1930

DIPARTIMENTO
DI SCIENZE DELLA TERRA
SAPIENZA
UNIVERSITÀ DI ROMA

An International Journal of
Mineralogy, Crystallography, Geochemistry,
Ore Deposits, Petrology, Volcanology
and applied topics on Environment, Archaeometry and Cultural Heritage

The crystal structure of mineral fibres. 2. Amosite and fibrous anthophyllite

Simone Pollastri [a,*], Natale Perchiazzi [b], Lara Gigli [c], Paolo Ferretti [d], Alessandro Cavallo [e], Nicola Bursi Gandolfi [a], Kilian Pollok [f], Alessandro F. Gualtieri [a]

[a] Department of Chemical and Geological Sciences, University of Modena and Reggio Emilia, Via Campi 103, I-41125 Modena, Italy
[b] Earth Sciences Department, University of Pisa, Via S. Maria 53, I-56126, Pisa, Italy
[c] Elettra-Sincrotrone Trieste S.C.p.A., Strada Statale 14 - km 163,5 in AREA Science Park, I-34149 Basovizza, Trieste, Italy
[d] Museum of Sciences, Via Calepina 14, I-38122 Trento, Italy
[e] Department of Earth and Environmental Sciences, University Milano-Bicocca, I-20126 Milano, Italy
[f] Institut für Geowissenschaften Mineralogie, Friedrich-Schiller-Universität Jena, Carl-Zeiss Promenade 10, D-07745 Jena, Germany

ARTICLE INFO

Submitted: January 2017
Accepted: January 2017
Available on line: March 2017

* Corresponding author:
simone.pollastri@unimore.it

DOI: 10.2451/2017PM693

How to cite this article:
Pollastri S. et al. (2017) Period. Mineral. 86, 55-65

ABSTRACT

This study reports for the first time crystal-structure data for amosite and fibrous anthophyllite. The chemical composition of the two fibre species was determined from EMPA. Crystal structures were refined using powder-diffraction data, using both laboratory sources and synchrotron radiation. Results were compared with the available literature data for the non-fibrous varieties grunerite and anthophyllite, respectively. The calculated site-occupancies for all samples are in agreement with the chemical compositions calculated from EMPA. The existing structure models of grunerite and orthorhombic anthophyllite also applies to the corresponding fibrous varieties amosite and fibrous anthophyllite, respectively. In amosite, both Fe^{2+} and Fe^{3+} atoms are found at the sites *M*(1), *M*(2) and *M*(3) and Fe^{2+} ions is the only atomic species found at site *M*(4). Mg is disordered over the C sites with a preference for site *M*(2). Minor Ca and Na have been assigned to the A site. In fibrous anthophyllite, Mg is the only atomic species found at the *M*1, *M*2 and *M*3 sites. Fe^{2+}, Mg (and minor Mn) have been assigned to the *M*4 site, whereas minor Ca has been assigned to the A site. In both structures, the environment at the *M*(4) site in amosite and *M*4 site in fibrous anthophyllite is highly distorted. This work can be considered a basis for studies aimed at understanding the potential toxicity/pathogenicity of these mineral fibres.

Keywords**:** Mineral fibres; amphibole; Rietveld; crystal-structure refinement; iron.

INTRODUCTION

Asbestos minerals (fibrous amphiboles and chrysotile; IARC, 1973; USGS, 2001) together with fibrous zeolites such as erionite, are the most common mineral fibres. The dreadful reputation of asbestos minerals is due to the onset of malignant lung diseases, mainly lung carcinoma and pleural/peritoneal malignant mesothelioma (MM), following their inhalation (see for reviews: Broaddus et al., 2011; Bunderson-Schelvan et al., 2011; Gulati and Redlich, 2015; Huang et al., 2011; Mossman et al., 2011; Roe and Stella, 2015). Despite the large number of studies over the last twenty years (see for example: Kamp, 2009; Huang et al., 2011; Liu et al., 2013; Mossman et al., 2011), the mechanisms by which asbestos, and mineral fibres in general, induce cyto- and geno-toxic damage remain poorly understood. This is due to their great chemical variability and atomic arrangements, in addition to other factors (fibre size, surface reactivity,

biopersistence, iron oxidation state/coordination number) that contribute to biogeochemical reactions (Fubini and Mollo, 1995; Hardy and Aust, 1995; Donaldson et al., 2010). This work is framed within the long-term research project entitled "*Sviluppo di un modello generale di interazioni tra fibre minerali e cellule biologiche*", part of the Italian Research Project of National Interest (PRIN), in progress since 2011, aimed at understanding the nature of biological interaction mechanisms of mineral fibres of socio-economic and industrial importance and to develop a general model of fibre toxicity. The model could be useful to assess the potential toxicity and pathogenicity of unclassified and unregulated fibres, preventing new cases of mass exposure such as those reported for the fluoro-edenite (Comba et al., 2003) and fibrous erionite (Dumortier et al., 2001). To achieve this goal, full mineralogical and crystallographic characterization of the fibres is of paramount importance and can be used as a basis to understand the chemical/physical and biological properties relevant to toxicity and pathogenicity.

Amphiboles are double-chain silicates with a Si(Al):O ratio of 4:11. The oxygen atoms of the chains can coordinate Si(Al) and also a variety of other cations sites; the simplified general formula for amphiboles, following Hawthorne et al. (2012) is: $A_{0\text{-}1}B_2C_5T_8O_{22}W_2$. The anions W (OH, F, Cl, O^{2-}) occur at the O(3) site, T (Si^{4+}, Al^{3+}) are the tetrahedrally coordinated sites within the silicate chain, the C cations (Mg^{2+}, Fe^{2+}, Mn^{2+}, Al^{3+}, Fe^{3+}, Ti^{3+}, Ti^{4+} Li^{+}, Mn^{3+}) occur at the octahedrally coordinated sites *M*(1), *M*(2) and *M*(3) in monoclinic amphiboles, the B cations (Na^{+}, Li^{+}, Ca^{2+}, Mn^{2+}, Fe^{2+}, Mg^{2+}) occur at the [8]-coordinated *M*(4) site in monoclinic amphiboles, and the A cations (Na^{+}, K^{+}, Ca^{2+}, Li^{+}) occur in the A cavity with coordination number from [6] to [12].

In the frame of the project, the chemical environment of iron in the crystal structure of these mineral fibres has been recently investigated (Pollastri et al., 2015) through a combined X-ray absorption and Mössbauer spectroscopic study. The results confirm that amphibole asbestos fibres host iron in octahedrally coordinated sites, in perfect agreement with previous studies (Whittaker, 1949; Bancroft et al., 1966; Whitfield and Freeman, 1967; Cameron and Papike, 1979; Stroink et al., 1980).

Our work is along the research line of the crystal chemical characterization of fibrous amphiboles such as fluoro-edenite (Gianfagna et al., 2003; Gianfagna et al., 2007; Andreozzi et al., 2009) fibrous tremolite (Ballirano et al., 2008; Pacella et al., 2008) fibrous richterite (Pacella and Ballirano, 2016) and winchite (Gunter et al., 2003).

This study reports for the first time crystal-structure data for amosite and fibrous anthophyllite, two of the fibrous amphiboles classified as asbestos so that all the structure models of the five amphibole asbestos species are now available. Samples were investigated by Electron Micro-Probe Analysis (EMPA) and X-Ray powder-diffraction (XRPD) experiments using both lab sources and synchrotron radiation. A special attention was paid to the occupancy of iron because it is considered to play a major role in the pathogenicity of the fibres, as it generates reactive oxygen species (ROS), mobilization by chelators and catalysed reactions (Hardy and Aust, 1995).

MATERIALS AND METHODS

Sample selection and preparation

The fibrous amphiboles selected for the study are:

- the UICC standard amosite asbestos (South African, NB #4173-111-4) (ideal formula $\square Fe^{2+}_2Fe^{2+}_5[Si_8O_{22}](OH)_2$ and space group C2/m) from Penge mine, Northern Province (South Africa)
- the UICC standard anthophyllite asbestos (Finnish NB #4173-111-5) (ideal formula $\square Mg_2Mg_5[Si_8O_{22}](OH)_2$ and space group Pnma) from Paakkila (Finland).

The surface reactivity, chemical environment of iron, thermal behaviour and trace elements in the samples have been already investigated by our group and published elsewhere (Pollastri et al., 2014; 2015; Bloise et al., 2015; 2016).

Samples were manually ground in agate mortar prior to the X-ray diffraction investigation.

Experimental and data analysis

EMPA were done using a JEOL 8200 Super Probe instrument with W hairpin-type filament and minimum accelerating voltage of 30 kV. The content of H_2O was independently determined on the very same samples with Thermogravimetric (TG) analysis (taken from the literature; Bloise et al., 2015). The final chemical compositions are the mean values of several analyses carried out on various fibres (not less than 10 per sample). The calculation of the crystal-chemical formula was normalized on the basis of 24 O. The assignment of Fe^{2+} and Fe^{3+} was possible using independent Mössbauer data (Pollastri et al., 2015). Cations reported in atoms per formula unit (a.p.f.u.) were assigned following the schemes proposed by Hawthorne et al. (2008) for anthophyllite and by Hawthorne and Oberti (2007) and Leake et al. (1997) for amosite.

High-resolution XRPD pattern of amosite was collected at the MS-X04SA beamline, SLS, Villigen, Switzerland. The beamline is powered by a short-period (14 mm) in-vacuum, cryogenically cooled, permanent-magnet undulator (CPMU, U14). The diffractometer has Debye-Scherrer geometry and is equipped with a solid-state silicon-microstrip detector, called MYTHEN (Microstrip sYstem for Time-rEsolved experimeNts). A detailed description of the beamline is reported in Willmott et al. (2013). The sample powder was inserted in a borosilicate capillary 0.3 mm in diameter and data were collected

by spinning the capillary. The wavelength used for the experiment was 0.775 Å.

The XRPD pattern of anthophyllite was collected using a conventional Bragg–Brentano PANalytical X'Pert Pro diffractometer, with Θ–Θ geometry, CuKα radiation, 40 kV and 40 mA and an RTMS (Real-Time Multiple-Strip) detector. The sample was side loaded on a zero-background sample-holder so to minimize preferred orientation. Data were collected in continuous mode with a 15 mm mask and 1/4° fixed divergence and antiscatter slits mounted in the incident beam, 0.02 rad soller slits on both incident and diffracted beam paths, and fixed 10 mm RTMS slit and a Ni filter in the diffracted beam path. An integrated step-scan of the RTMS detector of 0.0167 °2Θ was used with a time of 75 s/step from 3 to 120 °2Θ.

Preliminary quantitative phase analysis (for the identification of the impurities eventually present in the samples) were done using the Rietveld method (Rietveld, 1969) implemented in the GSAS package (Larson and Von Dreele, 1994) and its graphical interface EXPGUI (Toby, 2001). Rietveld structure refinements were done with the same software package, using starting coordinates taken from the literature (details and references are reported below). In GSAS, the structure factors were calculated using the formal scattering factors for neutral atoms. The background profile was fitted with a Chebyshev polynomial function with a variable number of coefficients depending on the complexity of the background curve. The diffraction peak profiles were modelled using a pseudo-Voigt function with a θ-independent Gaussian and two Lorentzian coefficients. The unit-cell parameters and phase fractions were refined together with the atom coordinates, the site occupancies, and isotropic atomic-displacement parameters. Soft constraints on T-site bond lengths were imposed and used as additional observations in the earlier stages of the refinement procedure. The weight of the constraints was progressively reduced in the later stages.

RESULTS AND DISCUSSION

The EMPA chemical compositions of the samples are reported in Table 1. These data, together with the H_2O content from TG analyses (Bloise et al., 2015) were used to calculate the relative crystal-chemical formulae.

Impurities were detected for each sample combining the EMPA results and the XRPD qualitative/quantitative phase analysis. Amosite contains calcite, hematite and quartz (all less than 1 wt%) whereas anthophyllite is contaminated with biotite [1.4(2) wt%], clinochlore/vermiculite [1.7(3) wt%] and talc [7.7(4) wt%].

Table 1. Chemical composition of samples from EMPA analysis. Reported chemical compositions are mean values of several analyses carried out on not less than 10 fibres per sample.

Oxides	Amosite	Fibrous anthophyllite
SiO_2	49.8(2)	57.3(4)
TiO_2	0.04(2)	0.02(2)
Al_2O_3	0.04(2)	0.11(5)
Cr_2O_3	0.01(1)	0.04(3)
MnO	0.42(6)	0.4(1)
FeO_{tot}	41.4(4)	9.9(7)
MgO	6.23(9)	28.5(2)
CaO	0.09(1)	0.27(7)
Na_2O	0.03(2)	0.02(1)
K_2O	0.02(1)	0.02(1)
NiO	0.02(4)	0.04(4)
Fe_2O_3*	3.9(4)	0.0
FeO*	37.8(4)	9.9(7)
H_2O**	1.94	2.60
Total	100.32	99.22
Sample	Chemical formula	
Amosite	$Ca_{0.02}Na_{0.01}Fe^{2+}_{2.00}(Fe^{2+}_{3.00}\ Fe^{3+}_{0.46}Mg_{1.47}Mn_{0.06})_{4.99}(Si_{7.86}{}^{IV}Al_{0.01})_{7.87}O_{21.96}(OH)_{2.04}$	
Fibrous anthophyllite	$Ca_{0.04}Mg_2(Mg_{3.83}Fe^{2+}_{1.14}Mn_{0.05})_{5.02}(Si_{7.86}{}^{IV}Al_{0.02})_{7.88}O_{21.62}(OH)_{2.38}$	

Note:* partition determined from Mössbauer data (Pollastri et al., 2015); **determined from TG data (Bloise et al., 2015).

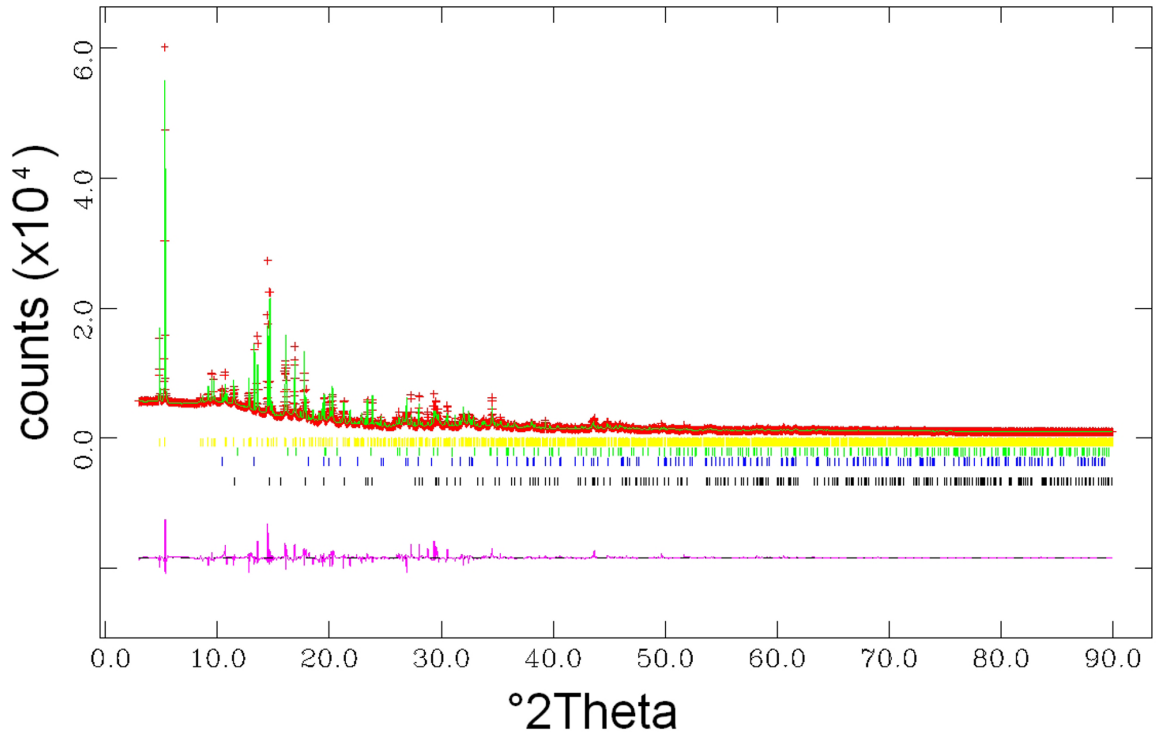

Figure 1a. Rietveld refinement of amosite. Observed (crosses), calculated (continuous green line), and difference (bottom violet line) curves are reported. Legend of the reflections markers, line from the bottom: calcite, quartz, hematite, amosite.

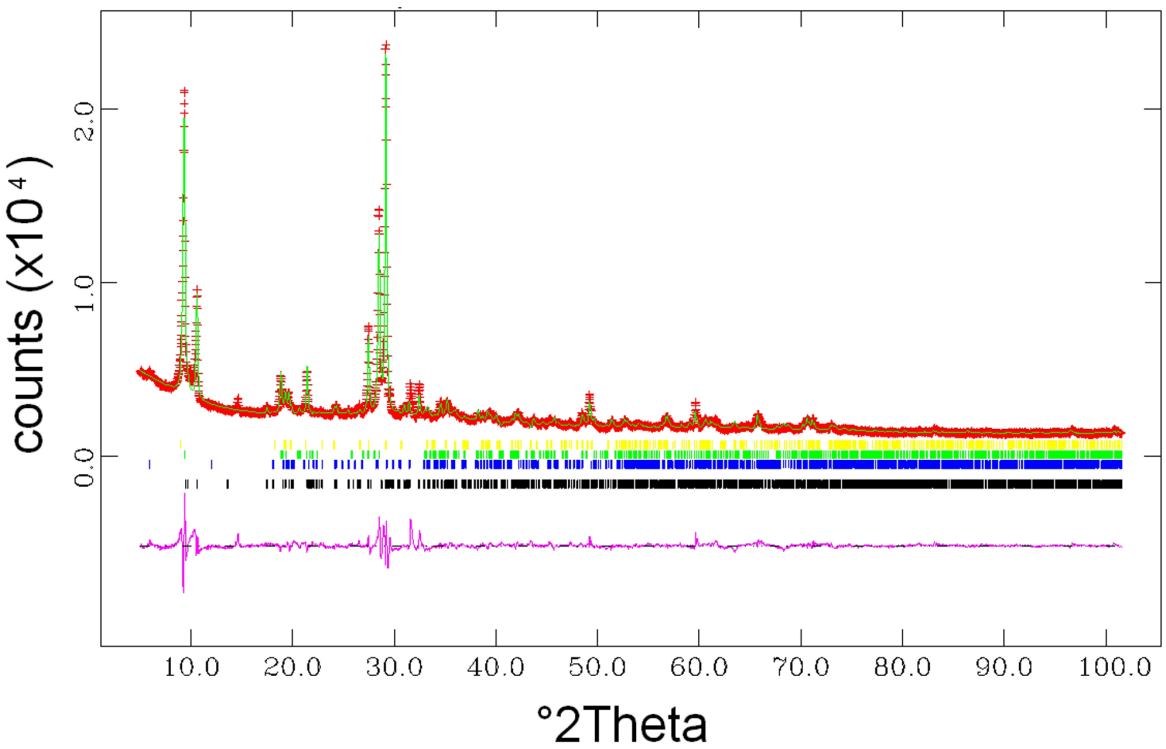

Figure 1b. Rietveld refinement of fibrous anthophyllite. Observed (crosses), calculated (continuous green line), and difference (bottom violet line) curves are reported. Legend of the reflections markers, line from the bottom: anthophyllite, clinochlore, talc, biotite.

Figure 1 a,b reports the graphical output of the fit obtained with Rietveld refinements for amosite and fibrous anthophyllite, respectively. The agreement factors of the refinements (as defined in Larson and Von Dreele, 1994) and calculated unit cell parameters are reported in Table 2. Fractional coordinates, isotropic displacement parameters ($Å^2$) and site scattering values obtained from the structure refinement are reported in Table 3 and 5 (for amosite and anthophyllite, respectively) whereas relative selected bond distances and polyhedral distortion ($\Delta \times 10^4$) for T and M sites are reported in Table 4 and 6 (for amosite and anthophyllite, respectively). For both samples, the refined site scattering values obtained from the structure refinement are in agreement with those calculated from the chemical compositions.

Amosite

The structure model of amosite, the fibrous variety of grunerite, is discussed in comparison with the grunerite model by Finger (1969), refined using a sample from Wabush Iron Formation, Labrador, Canada. All the refined cell parameters and volume (Table 2) are smaller than those of the grunerite model by Finger (1969) because of the lower iron content of our sample (Fe/Fe+Mg ratio is 0.88 for the Finger sample and 0.78 for our sample, respectively). Figure 2 is a plot modified after Hirschmann et al. (1994), showing the dependence of the unit cell parameters along the cummingtonite-grunerite series vs. Fe/Fe+Mg (%) ratio, with the indication of our sample (black star) and the Finger's sample (grey star).

The values of the <*T*-O> distances for both <*T*(1)-O> and <*T*(2)-O> are consistent with the literature values for virtually Al-free *C*2/*m* amphiboles (Hawthorne and Oberti, 2007). The geometry of the tetrahedra in amosite is very similar to that of Finger's grunerite with <*T*(1)-O>=1.628 Å (vs. 1.627 Å) and <*T*(2)-O>=1.633 Å (vs. 1.622 Å). Polyhedron distortion Δ shows very small values for both *T*(1) and *T*(2) tetrahedra (Table 4).

The results of the structure refinement indicate that Mg is disordered over the C sites with a preference for the *M*(2) site whereas Mg is not found at the B site *M*(4) (Table 3). This cation distribution scheme is in perfect agreement with the Finger's grunerite model where 15% Mg is found at the *M*(1) site, 22.7% at the *M*(2) site, 11.2% at the *M*(3) site and virtually no Mg at the *M*(4) site. Our cation distribution scheme is also in agreement with the single-crystal X-ray structure refinements of natural members of the cummingtonite-grunerite series (Ghose, 196l; Fischer, 1966; Finger, 1969; Ghose and Ganguly, 1982) showing that Fe^{2+} strongly prefers the *M*(4) site and Mg prefers *M*(2). The cation distribution scheme of amosite is also in agreement with the grunerite model of Ghose and Hellner (1959), where Mg and Fe are randomly distributed at the *M*(1), *M*(2), and *M*(3) sites and the *M*(4) site mainly occupied by iron.

The octahedrally coordinated cations at the *M*(1), *M*(2), and *M*(3) sites display a fairly regular environment. The mean <*M*(1,2,3)-O> is 2.084 Å and considering an empirical ionic radius of 0.78 Å for iron and 0.72 Å for magnesium in octahedrally coordinated environment, our data are in agreement with the estimated dependence of the <<*M*(1,2,3)-O>> distance as a function of the mean aggregate radius of the *M*(1,2,3) cations in *C*2/*m* amphiboles (Hawthorne and Oberti, 2007; see also Hirschmann et al., 1994).

Again, because of the lower iron content of our sample, <*M*(1,2,3)-O> distance is shorter than the value of 2.118 Å reported by Finger (1969) for grunerite.

The situation is clearly different for the *M*(4) site which occurs at the junction of the strip of octahedra and the double-chain of tetrahedra in all amphibole structure types, and is occupied by Fe^{2+} only in our sample. The B cation at the *M*(4) site bonds to oxygen atoms of both the strip of octahedra and the double chain of tetrahedra, and is the basic link between these two parts of the structure. As a result, this site and its constituent cations have a major influence on the symmetry, crystal chemistry and chemical composition of the amphiboles (Hawthorne and Oberti, 2007). The peculiarity of the site *M*(4) is also witnessed by the ordered Fe^{2+} magnetic moment at that site which is substantially lower than those at the other sites, most likely indicating strong covalency effects, i.e.

Table 2. Rietveld agreement factors (as defined in Larson and Von Dreele, 1994) and calculated unit cell parameters of amosite and fibrous anthophyllite.

sample	R_{wp}(%)	R_p(%)	χ^2	R_F^2(%)	Nr. observations	Refined parameters in the last stage of the refinement	Space group	a (Å)	b (Å)	c (Å)	β (°)
Amosite	8.23	5.00	5.44	18.58	3978	71	*C*2/*m*	9.5484(2)	18.3395(4)	5.3346(1)	101.825(2)
Fibrous anthophyllite	5.93	4.18	8.53	18.81	3072	108	*Pnma*	18.5770(8)	18.0353(22)	5.27285(9)	90

Table 3. Fractional coordinates, isotropic displacement parameters (Å^2) and site scattering values (in electrons per formula unit) obtained from the structure refinement of amosite. Populations the Rietveld refinement data are compared to those from the chemical data.

site	x/a	y/b	z/c	U_{iso}
T(1)	0.2839(4)	0.0860(2)	0.2640(8)	0.010(5)
T(2)	0.2945(4)	0.1671(2)	0.7729(8)	0.006(2)
M(1)	0	0.0881(3)	0.5	0.008(3)
M(2)	0	0.1745(3)	0	0.006(3)
M(3)	0	0	0	0.005(3)
M(4)	0	0.2545(4)	0.5	0.022(6)
O(1)	0.1096(4)	0.0868(2)	0.2023(8)	0.032(5)
O(2)	0.1182(4)	0.1713(2)	0.7116(7)	0.006(3)
O(3)	0.1090(8)	0	0.700(1)	0.005(2)
O(4)	0.422(1)	0.2282(4)	0.829(1)	0.040(5)
O(5)	0.336(1)	0.1435(4)	0.074(1)	0.005(3)
O(6)	0.343(1)	0.1346(4)	0.518(1)	0.005(3)
O(7)	0.320(1)	0	0.211(3)	0.007(3)

	Refinement	Site partition	Chemical data
M(1)	46.8	$Fe_{1.80(1)}$	
	2.4	$Mg_{0.20(1)}$	
M(2)	35.4	$Fe_{1.36(2)}$	
	7.7	$Mg_{0.64(2)}$	
M(3)	22.6	$Fe_{0.87(2)}$	
	1.6	$Mg_{0.13(2)}$	
C sites sum	116.5		109.1
M(4)	52	$Fe^{2+}_{2.00}$	52
B site sum	52		52
A site	0.4	$Ca_{0.02}$	0.4
	0.11	$Na_{0.01}$	0.11
A site sum	0.51		0.51

Table 4 - Selected bond distances (in Å) and polyhedral distortion ($\Delta\times10^4$) for T and M sites in amosite.

T(1)-O(1)	1.629(6)	T(2)-O(2)	1.649(5)				
T(1)-O(5)	1.610(5)	T(2)-O(4)	1.639(5)				
T(1)-O(6)	1.622(6)	T(2)-O(5)	1.633(5)				
T(1)-O(7)	1.651(5)	T(2)-O(6)	1.635(6)				
<T(1)-O>	1.628	<T(2)-O>	1.633				
Δ	0.839	Δ	0.278				
M(1)-O(1)×2	2.073(9)	*M*(2)-O(1)×2	2.09(1)	*M*(3)-O(1)×4	2.082(9)	*M*(4)-O(2)×2	2.087(9)
M(1)-O(2)×2	2.087(9)	*M*(2)-O(2)×2	2.09(1)	*M*(3)-O(3)×2	2.080(8)	*M*(4)-O(4)×2	2.06(1)
M(1)-O(3)×2	2.091(9)	*M*(2)-O(4)×2	2.072(9)			*M*(4)-O(6)×2	2.54(1)
<*M*(1)-O>	2.088	<*M*(2)-O>	2.084	<*M*(3)-O>	2.081	<*M*(4)-O>	2.233
Δ	0.180	Δ	0.166	Δ	0.002	Δ	97.263

Note: *Polyhedron distortion Δ as defined by Brown and Shannon (1973): $\Delta= (1/n)\Sigma[(R_i-R)/R]^2$ where n is the number of ligands. R is the average bond length and R_i an individual bond length.

Table 5. Fractional coordinates, isotropic displacement parameters (Å^2) and site scattering values (in electrons per formula unit) obtained from the structure refinement of anthophyllite. Populations the Rietveld refinement data are compared to those from the chemical data.

site	x/a	y/b	z/c	U_{iso}
*T*1A	0.2305(9)	-0.1628(9)	-0.455(7)	0.02(1)
*T*1B	0.0216(9)	-0.166(1)	0.291(6)	0.03(1)
*T*2A	0.224(1)	-0.086(2)	0.083(7)	0.05(1)
*T*2B	0.020(1)	-0.089(1)	-0.246(6)	0.01(1)
*M*1	0.133(1)	0.1501(8)	0.408(6)	0.03(1)
*M*2	0.123(1)	0.077(1)	-0.103(6)	0.05(1)
*M*3	0.128(2)	¼	-0.145(7)	0.03(1)
*M*4	0.123(1)	-0.013(1)	0.414(4)	0.004(9)
O1A	0.1822(9)	0.166(2)	0.051(6)	0.006(9)
O1B	0.0655(9)	0.163(2)	-0.277(6)	0.005(9)
O2A	0.191(1)	0.067(1)	-0.417(6)	0.03(1)
O2B	0.066(1)	0.073(1)	0.236(5)	0.02(1)
O3A	0.182(2)	¼	-0.486(8)	0.004(9)
O3B	0.131(3)	¼	0.240(8)	0.04(1)
O4A	0.175(2)	-0.013(2)	0.068(6)	0.04(1)
O4B	0.068(2)	-0.015(2)	-0.247(5)	0.005(9)
O5A	0.186(1)	-0.122(2)	0.327(4)	0.01(1)
O5B	0.038(2)	-0.130(3)	0.017(5)	0.02(1)
O6A	0.210(2)	-0.129(3)	-0.181(4)	0.02(1)
O6B	0.058(2)	-0.145(2)	-0.441(3)	0.03(1)
O7A	0.213(3)	¾	0.52(2)	0.03(1)
O7B	0.045(3)	¾	0.23(2)	0.02(1)
	Refinement	Site partition		Chemical data
*M*1	24	$Mg_{2.00}$		24
*M*2	24	$Mg_{2.00}$		24
*M*3	12	$Mg_{1.00}$		12
C sites sum	60			60
	9.12	$Mg_{0.76}$		9.96
M4	32.24	$Fe^{2+}_{1.24}$		29.64
	2.5	$Mn_{0.1}$		2.5
B site sum	43.9			42.1
A site	0.8	$Ca_{0.04}$		0.8
A site sum	0.8			0.8

considerable spin transfer to neighboring oxygen atoms (Ghose et al., 1987).

The distance <*M*(4)-O>=2.223 Å of amosite is comparable to that of the Finger's grunerite (2.293 Å), although the latter includes unrealistic values such as the distance *M*(4)-O(4) of 1.988(4) Å. It is confirmed that <*M*(4)-O> increases lightly in the cummingtonite-grunerite series with macroscopic Fe/(Fe+Mg), primarily owing to large changes in the longer *M*(4)-O6 distance. It is also confirmed that the *M*(4)-O4 bond distance actually decreases with increasing Fe/(Fe + Mg), which is consistent with the inference that this bond has considerable covalent character (Ghose and Ganguly, 1982). The octahedral environment of Fe^{2+} at the *M*(4) site

Table 6. Selected bond distances (in Å) and polyhedral distortion ($\Delta \times 10^4$) for T and M sites in fibrous anthophyllite.

*T*1A-O1A	1.624(6)	*T*2A-O2A	1.611(6)	*T*1B-O1B	1.620(6)	*T*2B-O2B	1.614(6)
*T*1A-O5A	1.603(6)	*T*2A-O4A	1.609(6)	*T*1B-O5B	1.607(6)	*T*2B-O4B	1.608(6)
*T*1A-O6A	1.612(6)	*T*2A-O5A	1.604(6)	*T*1B-O6B	1.607(6)	*T*2B-O5B	1.610(6)
*T*1A-O7A	1.612(6)	*T*2A-O6A	1.612(6)	*T*1B-O7B	1.613(6)	*T*2B-O6B	1.606(6)
<*T*1A-O>	1.613	<*T*2A-O>	1.609	<*T*1B-O>	1.612	<*T*2B-O>	1.610
Δ	0.214	Δ	0.037	Δ	0.111	Δ	0.035
*M*1-O1A	2.11(1)	*M*2-O1A	2.11(1)	*M*3-O1A×2	2.085(8)	*M*4-O2A	2.109(6)
*M*1-O1B	2.10(1)	*M*2-O1B	2.10(1)	*M*3-O1B×2	2.072(8)	*M*4-O2B	2.109(6)
*M*1-O2A	2.06(1)	*M*2-O2A	2.09(1)	*M*3-O3A	2.05(1)	*M*4-O4A	2.064(4)
*M*1-O2B	2.08(1)	*M*2-O2B	2.08(1)	*M*3-O3B	2.03(1)	*M*4-O4B	2.060(4)
*M*1-O3A	2.09(1)	*M*2-O4A	2.09(1)			*M*4-O5A	2.33(1)
*M*1-O3B	2.01(1)	*M*2-O4B	2.10(1)			*M*4-O6B	2.79(1)
<*M*1-O>	2.074	<*M*2-O>	2.095	<*M*3-O>	2.066	<*M*4-O>	2.244
Δ	2.540	Δ	0.209	Δ	0.916	Δ	135.1

Note: *Polyhedron distortion Δ as defined by Brown and Shannon (1973): $\Delta = (1/n)\Sigma[(R_i-R)/R]^2$ where n is the number of ligands. R is the average bond length and R_i an individual bond length.

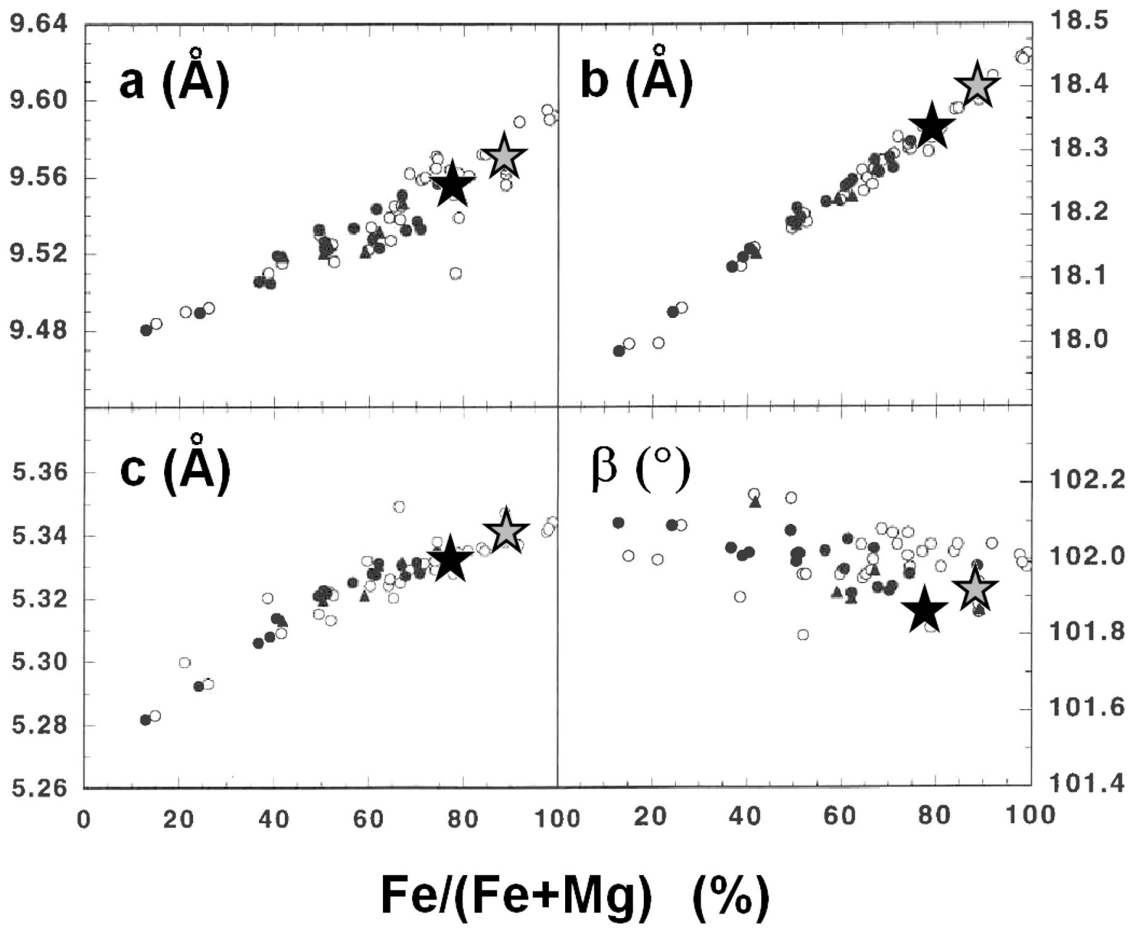

Figure 2. Figure modified after Hirschmann et al. (1994), showing the dependence of the unit cell parameters along the cummingtonite-grunerite series vs. Fe/Fe+Mg (%) ratio. Legend: grey star= Finger's grunerite; black star= our amosite sample.

is highly distorted as witnessed by the enormous value of the polyhedron distortion (Δ=97.263). Such value is even greater for the Finger's grunerite (211.294).

Fibrous anthophyllite

This is the first published structure refinement of fibrous anthophyllite, as literature reports only structure models of non-fibrous orthorhombic anthophyllites (Warren and Modell, 1930; Lindemann, 1964; Finger, 1970; Walitzi et al., 1989; Evans et al., 2001; Schindler et al., 2008; Hawthorne et al., 2008). The results of our structure refinement (Table 2, 5, and 6) will be compared to those of the fully characterized samples by Walitzi et al. (1989), Schindler et al. (2008), and Hawthorne et al. (2008). The samples studied by these authors share many crystal-chemical features with our sample: they are Al-poor (Al is <0.5 a.p.f.u.); they display no Fe^{3+}; Fe^{2+} is in the range 1.14-1.66 a.p.f.u. (our sample has the lowest Fe^{2+} content); they possess comparable unit cell dimensions, with 18.544 ≤ *a* (Å) ≤ 18.577, 18.026 ≤ *b* (Å) ≤ 18.353, and 5.273 ≤ *c* (Å) ≤ 5.290.

The values of the mean <*T*-O> distance of 1.611 Å for our fibrous anthophyllite (with Al=0.01 a.p.f.u.) is in very good agreement with the grand <T-O> distance of 1.621(1) Å for virtually $^{[4]}$Al-free *Pnma* amphiboles (Schindler et al., 2008) and with the anthophyllite of Walitzi et al. (1989) having Al=0.5 a.p.f.u. and <*T*-O>=1.625 Å. Polyhedron distortion Δ shows very small values for all the tetrahedra (Table 6).

The results of the structure refinement indicate that Mg only is found at the *M*1, *M*2 and *M*3 sites with Fe^{2+} at the *M*4 together with Mn, and minor Ca at the A site (Table 5). This result is virtually identical to that found by Walitzi et al. (1989) for their orthorhombic anthophyllite. Schindler et al. (2008) also assigned most of Fe^{2+} (1.02-1.39 a.p.f.u.) to *M*4 with minor populations at the *M*1 (0.17-0.32 a.p.f.u.), *M*2 (0.04-0.17 a.p.f.u.), and *M*3 (0.05-0.14 a.p.f.u.) sites in orthorhombic anthophyllites. The octahedrally coordinated Mg at the *M*1, *M*2, and *M*3 sites display a regular geometry as the polyhedron distortion Δ shows small values for all the octahedra (Table 6). The mean <*M*1,2,3-O> is 2.078 Å and considering an empirical ionic radius of 0.72 Å for magnesium in octahedrally coordinated environment, our data are in agreement with the estimated dependence of the <<*M*1,2,3-O>> distance as a function of the mean aggregate radius of the *M*(1,2,3) cations in Figure 6 of Schindler et al. (2008).

Site *M*4 shows some differences with respect to the literature data. The distance <*M*4-O>=2.244 Å for a 6-fold coordination is comparable to the value (2.261 Å) reported by Walitzi et al. (1989) for their anthophyllite with *M*4 in an octahedrally coordinated environment. Such distances are shorter with respect to the values reported by Schindler et al. (2008) for orthorhombic anthophyllite with *M*4 in a 7-fold coordinated environment: <$^{[7]}$*M*4-O>=2.349(2) Å for sample A(5) and 2.351(3) Å for sample A(18) (see Table 5a,b in Schindler et al., 2008). The octahedral environment at the *M*4 site is highly distorted as witnessed by the enormous value of the polyhedron distortion (Δ=135.1).

CONCLUSIONS

The results of our structure refinements confirm that the existing structure models of grunerite and orthorhombic anthophyllite also applies to the corresponding fibrous varieties amosite and fibrous anthophyllite, respectively. In amosite, both Fe^{2+} and Fe^{3+} atoms are found at the *M*(1), *M*(2) and *M*(3) sites and Fe^{2+} ions is the only atomic species found at site *M*(4). Mg is disordered over the C sites with a preference for site *M*(2). Minor Ca and Na have been assigned to the A site.

For fibrous anthophyllite, Mg is the only atomic species found at the *M*1, *M*2 and *M*3 sites. Fe^{2+}, Mg and minor Mn have been assigned to the *M*4 site, whereas minor Ca has been assigned to the A site. In both structures, the environment at the *M*(4) site for amosite and *M*4 site in fibrous anthophyllite is highly distorted.

Our results are consistent with the findings of our previous X-ray absorption and Mössbauer spectroscopic study (Pollastri et al., 2015) indicating that all amphibole asbestos fibres host iron exclusively in octahedrally coordinated sites. The knowledge of the positions of Fe atoms within the crystal structure is of help to understand the toxicity/pathogenicity of mineral fibres.

ACKNOWLEDGMENTS

This research was done within the research project "Sviluppo di un modello generale di interazioni tra fibre minerali e cellule biologiche", part of the comprehensive long-term Italian Research Project of National Interest (PRIN 2011) entitled "Interazione fra minerali e biosfera: conseguenze per l'ambiente e la salute umana". This work was also financially supported by the University of Pisa through the project P.R.A. 2016 "Ruolo di zone di taglio nella costruzione degli orogeni: case histories da catene orogenetiche". Synchrotron XRPD of amosite was collected at the MS-X04SA beamline at SLS (Villigen, Switzerland) under the beam-time allocated for the experiment 20130049 (July 2013). We thank Prof. Stefano Poli and Dott. Andrea Risplendente for the EMPA. This work benefited the careful revision of Frank C. Hawthorne and two anonymous referees. We warmly acknowledged them for their careful and indispensable contribution that substantially improved the quality of the final version of the manuscript.

REFERENCES

Andreozzi G.B., Ballirano P., Gianfagna A., Mazziotti Tagliani S., Pacella A., 2009. Structural and spectroscopic characterization of a suite of fibrous amphiboles with high

environmental and health relevance from Biancavilla (Sicily, Italy). American Mineralogist 94, 1333-1340.

Ballirano P., Andreozzi G.B., Belardi G., 2008. Crystal chemical and structural characterization of fibrous tremolite from Susa Valley, Italy, with comments on potential harmful effects on human health. American Mineralogist 93, 1349-1355.

Bancroft G.M., Maddock A.G., Burns R.G., Strens R.G.J., 1966. Cation distribution in anthophyllite from Mössbauer and infra-red spectroscopy. Nature 212, 913-915.

Bloise A., Barca D., Gualtieri A.F., Pollastri S., Belluso E., 2016. Trace elements in hazardous mineral fibres. Environmental Pollution 216, 314-323.

Bloise A., Catalano M., Barrese E., Gualtieri A. F., Gandolfi N. B., Capella S., Belluso E., 2015. TG/DSC study of the thermal behaviour of hazardous mineral fibres. Journal of Thermal Analysis and Calorimetry 1-15.

Broaddus V.C., Everitt J.I., Black B., Kane A.B., 2011. Non-neoplastic and neoplastic pleural endpoints following fiber exposure. Journal of toxicology and environmental health Part B, Critical reviews 14, 153-178.

Brown I.T. and Shannon R.D., 1973. Empirical bond-strength–bond-length curves for oxides. Acta Crystallographica Section A: Crystal Physics, Diffraction, Theoretical and General Crystallography 29(3), 266-282.

Bunderson-Schelvan M., Pfau J.C., Crouch R., Holian A., 2011. Nonpulmonary outcomes of asbestos exposure. Journal of toxicology and environmental health Part B, Critical reviews 14, 122-152.

Cameron M. and Papike J. J., 1979. Amphibole crystal chemistry: A review. Fortschritte der Mineralogie 57, 28-67.

Comba P., Gianfagna A., Paoletti L., 2003) Pleural mesothelioma cases in Biancavilla are related to a new fluoro-edenite fibrous amphibole. Archives of Environmental Health: An International Journal 58, 229-232.

Donaldson K., Murphy F. A., Duffin R., Poland C. A., 2010. Asbestos, carbon nanotubes and the pleural mesothelium: a review of the hypothesis regarding the role of long fibre retention in the parietal pleura, inflammation and mesothelioma. Particle and Fibre Toxicology 7, 1-17.

Dumortier P., Coplü L., Broucke I., Emri S., Selcuk T., De Maertelaer V., De Vuist P., Baris I., 2001. Erionite bodies and fibres in bronchoalveolar lavage fluid (BALF) of residents from Tuzköy, Cappadocia, Turkey. Occupational and Environmental Medicine 58, 261-266.

Evans B.W., Ghiorso M.S., Yang H., Medenbach O., 2001. Thermodynamics of the amphiboles: Anthophyllite-ferroanthophyllite and the ortho-clino phase loop. American Mineralogist 86(5-6), 640-651.

Fischer K.F., 1966. A further refinement of the crystal structure of cummingtonite, $(Mg,Fe)_7(Si_4O_{11})_2(OH)_2$. American Mineralogist 51, 814-818.

Finger L.W., 1969. The crystal structure and cation distribution of a grunerite. Mineralogical Society of America Special Paper 2, 95-100.

Finger L.W., 1970. Refinement of the crystal structure of an anthophyllite. Carnegie Institute of Washington Year Book 68, 283-288.

Fubini B. and Mollo L., 1995. Role of iron in the reactivity of mineral fibers. Toxicology Letters 82, 951-960.

Ghose S., 1961. The crystal structure of a cummingtonite. Acta Crystallographica 14(6), 622-627.

Ghose S., Cox D. E., Van Dang N., 1987. Magnetic order in grunerite, $Fe_7Si_8O_{22}(OH)_2$. A quasi-one dimensional antiferromagnet with a spin canting transition. Physics and Chemistry of Minerals 14(1), 36-44.

Ghose S. and Ganguly J., 1982. Mg-Fe order-disorder in ferromagnesian silicates. In Advances in physical geochemistry Springer New York 3-99.

Ghose S. and Hellner E., 1959. The Crystal Structure of Grunerite and Observations on the Mg-Fe Distribution. The Journal of Geology 67, 691-701.

Gianfagna A., Andreozzi G. B., Ballirano P., Mazziotti-Tagliani S., Bruni B. M., 2007. Crystal chemistry of the new fibrous fluoro-edenite amphibole of volcanic origin from Biancavilla (Sicily, Italy). Canadian Mineralogist *45*, 249-262.

Gianfagna A., Ballirano P., Bellatreccia F., Bruni B., Paoletti L., Oberti R., 2003. Characterization of amphibole fibres linked to mesothelioma in the area of Biancavilla, Eastern Sicily, Italy. Mineralogical Magazine *67*(6), 1221-1229.

Gulati M. and Redlich C.A., 2015. Asbestosis and environmental causes of usual interstitial pneumonia. Current opinion in pulmonary medicine 21, 193-200.

Gunter M.E., Dyar M.D., Twamley B., Foit F.F. Jr., Cornelius C., 2003. Composition, Fe^{3+}/SFe, and crystal structure of nonasbestiform and asbestiform amphiboles from Libby, Montana, U.S.A. American Mineralogist 88, 1970-1978.

Hardy J.A. and Aust A.E., 1995.. Iron in asbestos chemistry and carcinogenicity. Chemical Reviews 95, 97-118.

Hawthorne F.C. and Oberti R., 2007. Amphiboles: crystal chemistry. In: Reviews in Mineralogy and Geochemistry, The Mineralogical Society of America and The Geochemical Society 67(1), 1-54.

Hawthorne F.C., Schindler M., Abdu Y., Sokolova E., Evans B.W., Ishida K., 2008. The crystal chemistry of the gedrite-group amphiboles. II. Stereochemistry and chemical relations. Mineralogical Magazine 72, 731-745.

Hawthorne F. C., Oberti R., Harlow G. E., Maresch W.V., Martin R.F., Schumacher J.C., Welch M.D., 2012. Nomenclature of the amphibole supergroup. American Mineralogist, 97, 2031-2048.

Hirschmann M., Evans B.W., Hexiong Y., 1994. Composition and temperature dependence of Fe-Mg ordering in cummingtonite-grunerite as determined by X-ray diffraction. American Mineralogist, 79, 862-377.

Huang S.X., Jaurand M.C., Kamp D.W., Whysner J., Hei T.K., 2011. Role of mutagenicity in asbestos fiber-induced carcinogenicity and other diseases. Journal of toxicology and environmental health Part B, Critical reviews 14, 179-245.

IARC, 1973. Some inorganic and organometallic compounds. IARC Monogr. Eval. Carcinog. Risk Chem. Man 2, 1-181.

Kamp D.W., 2009. Asbestos-induced lung diseases: an update. Translational research : the journal of laboratory and clinical medicine 153, 143-152.

Larson A.C. and Von Dreele R.B., 1994. Generalized Structure Analysis System. Los Alamos National Lab, New Mexico, LAUR 86-748.

Leake B.E., Woolley A.R., Arps C.E.S., Birch W.D., Gilbert M.C., Grice J.D., Hawthorne F.C., Kato A., Kisch H.J., Krivovichev V.G., Linthout K., Laird J., Mandarino J.A., Maresch V.W., Nickel E.H., Rock N.M.S., Schumacher

J.C., Smith D.C., Stephenson N.N., Ungaretti L., Withtaker E.J.W., Youzhi G., 1997. Nomenclature of amphiboles: report of the subcommittee on amphiboles of the International Mineralogical Association, Commission on New Minerals and Mineral Names. American Mineralogist 82, 1019-1037.

Lindemann W., 1964. Beitrag zur Struktur des Anthophyllits. Fortschritte der Mineralogie 42, 205 (abstract).

Liu G., Cheresh P. Kamp D.W., 2013. Molecular basis of asbestos-induced lung disease. Annual Review of Pathology 8, 161-187.

Mossman B.T., Lippmann M., Hesterberg T.W., Kelsey K.T., Barchowsky A. Bonner J.C., 2011. Pulmonary endpoints (lung carcinomas and asbestosis) following inhalation exposure to asbestos. Journal of Toxicology and Environmental Health Part B, Critical reviews 14, 76-121.

Pacella A., Andreozzi G.B., Ballirano P. Gianfagna A., 2008. Crystal chemical and structural characterization of fibrous tremolite from Ala di Stura (Lanzo Valley, Italy). Periodico di Mineralogia 77, 51-62.

Pacella A. and Ballirano P., 2016. Chemical and structural characterization of fibrous richterite with high environmental and health relevance from Libby, Montana (USA). Periodico di Mineralogia 85, 169-177

Pollastri S., Gualtieri A.F., Gualtieri M.L., Hanuskova M., Cavallo A., Gaudino G., 2014. The zeta potential of mineral fibres. Journal of Hazardous Materials 276, 469-479.

Pollastri S., D'Acapito F., Trapananti A., Colantoni I., Andreozzi G.B., Gualtieri A.F., 2015. The chemical environment of iron in mineral fibres. A combined X-ray absorption and Mössbauer spectroscopic study. *J*ournal of Hazardous Materials 298, 282-293.

Rietveld H.M., 1969. A profile refinement method for nuclear and magnetic structures. Journal of Applied Crystallography 2, 65-71.

Roe O.D. and Stella G.M., 2015. Malignant pleural mesothelioma: history, controversy and future of a manmade epidemic. European respiratory review: an official journal of the European Respiratory Society 24, 115-131.

Schindler M., Sokolova E., Abdu Y., Hawthorne F.C., Evans B.W. Ishida K., 2008. The crystal chemistry of the gedrite-group amphiboles. I. Crystal structure and site populations. Mineralogical Magazine 72, 703-730.

Stroink G., Blaauw C., White C.G., Leiper W., 1980. Mössbauer characteristics of UICC standard reference asbestos samples. The Canadian Mineralogist 18, 285-290.

Toby B.H., 2001. EXPGUI, a graphical user interface for GSAS. Journal of Applied Crystallography 34, 210-213.

USGS, 2001. Some Facts about Asbestos (USGS Fact Sheet FS-012-01) 4 pp.

Walitzi E.M., Walter F., Ettinger K., 1989. Verfeinerung der kristallstruktur von anthophyllit vom Ochsenkogel/Gleinalpe, Osterreich. Zeitschrift für Kristallographie 188, 237-244.

Warren B. and Modell D., 1930. The structure of Anthophyllite $H_2Mg_7(SiO_3)_8$. Zeitschrift für Kristallographie,75, 161-179.

Whitfield H.J. and Freeman A.G., 1967. Mössbauer study of amphiboles. Journal of Inorganic and Nuclear Chemistry 29, 903-914.

Whittaker E.J.W., 1949. The structure of Bolivian crocidolite. Acta Crystallographica 2, 312-317.

Willmott P.R., Meister D., Leake S.J., Lange M., Bergamaschi A., Böge M., Calvi M., Cancellieri C., Casati N., Cervellino A., Chen Q., David C., Flechsig U., Gozzo F., Henrich B., Jäggi-Spielmann S., Jakob B., Kalichava I., Karvinen P., Krempasky J., Lüdeke A., Lüscher R., Maag S., Quitmann C., Reinle-Schmitt M. L., Schmidt T., Schmitt B., Streun A., Vartiainen I., Vitins M., Wang X., Wullschleger R., 2013. The materials science beamline upgrade at the Swiss Light Source. Journal of Synchrotron Radiation 20, 667-682.